BIOCHEMISTRY
including biophysical chemistry & molecular biology
Article

Biochemistry **2011,** *50,* 1403–1411 1403
DOI: 10.1021/bi101319v

Use of 2,3,5-F_3Y-β2 and 3-NH_2Y-α2 To Study Proton-Coupled Electron Transfer in *Escherichia coli* Ribonucleotide Reductase[†]

Mohammad R. Seyedsayamdost,[‡,∥] Cyril S. Yee,[‡] and JoAnne Stubbe*[,‡,§]

[‡]*Department of Chemistry and* [§]*Department of Biology, Massachusetts Institute of Technology, 77 Massachusetts Avenue, Cambridge, Massachusetts 02139-4307, United States.* [∥]*Current address: Department of Biological Chemistry and Molecular Pharmacology, Harvard Medical School, 240 Longwood Avenue, Boston, Massachusetts 02115.*

Received August 17, 2010; Revised Manuscript Received November 29, 2010

ABSTRACT: *Escherichia coli* ribonucleotide reductase is an α2β2 complex that catalyzes the conversion of nucleoside 5′-diphosphates (NDPs) to deoxynucleotides (dNDPs). The active site for NDP reduction resides in α2, and the essential diferric-tyrosyl radical ($Y_{122}^{\bullet}$) cofactor that initiates transfer of the radical to the active site cysteine in α2 (C_{439}), 35 Å removed, is in β2. The oxidation is proposed to involve a hopping mechanism through aromatic amino acids ($Y_{122} \rightarrow W_{48} \rightarrow Y_{356}$ in β2 to $Y_{731} \rightarrow Y_{730} \rightarrow C_{439}$ in α2) and reversible proton-coupled electron transfer (PCET). Recently, 2,3,5-F_3Y (F_3Y) was site-specifically incorporated in place of Y_{356} in β2 and 3-NH_2Y (NH_2Y) in place of Y_{731} and Y_{730} in α2. A pH−rate profile with F_3Y_{356}-β2 suggested that as the pH is elevated, the rate-determining step of RNR can be altered from a conformational change to PCET and that the altered driving force for F_3Y oxidation, by residues adjacent to it in the pathway, is responsible for this change. Studies with $NH_2Y_{731(730)}$-α2, β2, CDP, and ATP resulted in detection of NH_2Y radical ($NH_2Y^{\bullet}$) intermediates capable of dNDP formation. In this study, the reaction of F_3Y_{356}-β2, α2, CDP, and ATP has been examined by stopped-flow (SF) absorption and rapid freeze quench electron paramagnetic resonance spectroscopy and has failed to reveal any radical intermediates. The reaction of F_3Y_{356}-β2, CDP, and ATP has also been examined with NH_2Y_{731}-α2 (or NH_2Y_{730}-α2) by SF kinetics from pH 6.5 to 9.2 and exhibited rate constants for $NH_2Y^{\bullet}$ formation that support a change in the rate-limiting step at elevated pH. The results together with kinetic simulations provide a guide for future studies to detect radical intermediates in the pathway.

Ribonucleotide reductases (RNRs)[1] are responsible for reduction of nucleotides to 2′-deoxynucleotides (dNDPs), supplying the precursors required for DNA replication and repair (*1*, *2*). Active *Escherichia coli* RNR is a 1:1 complex of two homodimeric subunits, α2 and β2 (*3*−*5*). α2 harbors the active site, where thiyl radical-mediated ($C_{439}^{\bullet}$) nucleotide reduction occurs (*6*−*8*), and the binding sites for allosteric effectors, which control the rate and specificity of reduction (*9*). β2 houses the essential diferric-tyrosyl radical ($Y_{122}^{\bullet}$) cofactor (*10*, *11*). Each turnover requires oxidation of C_{439} in α2 by $Y_{122}^{\bullet}$ in β2 (*12*). A structure of the active α2β2 complex is unavailable. However, a docking model of this complex, based on shape complementarity of the structures of the individual subunits, led Uhlin and Eklund to propose that transfer of a radical between subunits occurs over a distance of 35 Å by a pathway involving aromatic amino acid radicals (Figure 1A,B) (*13*). Mutagenesis studies suggested that the residues shown in panels A and B of Figure 1 are important for catalysis (*14*−*16*). The inactivity of the mutants, however, precluded mechanistic studies. We have recently incorporated unnatural amino acids site-specifically into the pathway. Our studies have provided direct evidence for the three proposed redox-active tyrosines (Y_{356}, Y_{731}, and Y_{730}) (*17*−*19*), the pathway dependence (*20*), and the docking model (*21*). In the study presented here, we investigate 2,3,5-F_3Y (F_3Y) site-specifically incorporated in place of Y_{356} in β2 with wild-type α2 (wt-α2) and with 3-NH_2Y (NH_2Y) incorporated site-specifically in place of Y_{731} or Y_{730} in α2 (Figure 1A,B) using rapid freeze quench (RFQ) EPR and stopped-flow (SF) absorption spectroscopies. These studies provide evidence that altering the driving force for oxidation of F_3Y_{356} by adjacent residues in the pathway via an increase in pH can change the rate-limiting step of RNR from a conformational change to proton-coupled electron transfer (PCET) and that no radical intermediates are detected.

Y analogues with altered reduction potentials and/or pK_a values were of interest for site-specific incorporation into RNR, as oxidation of Y is a PCET process with peak potentials (E_p) being modulated by pH (Figure 1C) (*22*−*24*). Studies of blocked F_nY analogues, N-acetylated and C-amidated, revealed the appropriateness of these analogues for studying PCET as their

[†]We thank the National Institutes of Health (Grant 29595 to J.S.) for support of this work. M.R.S. is a Novartis Fellow of the Life Sciences Research Foundation.

*To whom correspondence should be addressed. Telephone: (617) 253-1814. E-mail: stubbe@mit.edu.

[1]Abbreviations: α, ribonucleotide reductase large subunit; β, ribonucleotide reductase small subunit; $C^{\bullet}$, thiyl radical; CDP, cytidine 5′-diphosphate; DOPA, 3,4-dihydroxyphenylalanine (or 3-hydroxytyrosine); DTT, dithiothreitol; EDTA, ethylenediaminetetraacetic acid; EPL, expressed protein ligation; EPR, electron paramagnetic resonance; ET, electron transfer; F_3Y, 2,3,5-trifluorotyrosine; intein wt-β2, $V_{353}G/S_{354}C$-β2 generated by EPL; k_{fwd}, forward rate constant; k_{obs}, observed rate constant; k_{rev}, reverse rate constant; NDP, nucleoside 5′-diphosphate; NH_2Y, 3-aminotyrosine; $NH_2Y^{\bullet}$, 3-aminotyrosyl radical; PCET, proton-coupled electron transfer; RFQ, rapid freeze quench; RNR, ribonucleotide reductase; SF, stopped-flow; TR, thioredoxin; TRR, thioredoxin reductase; $W^{\bullet}$, tryptophan radical; wt, wild-type; $Y^{\bullet}$, tyrosyl radical.

Published on Web 12/23/2010

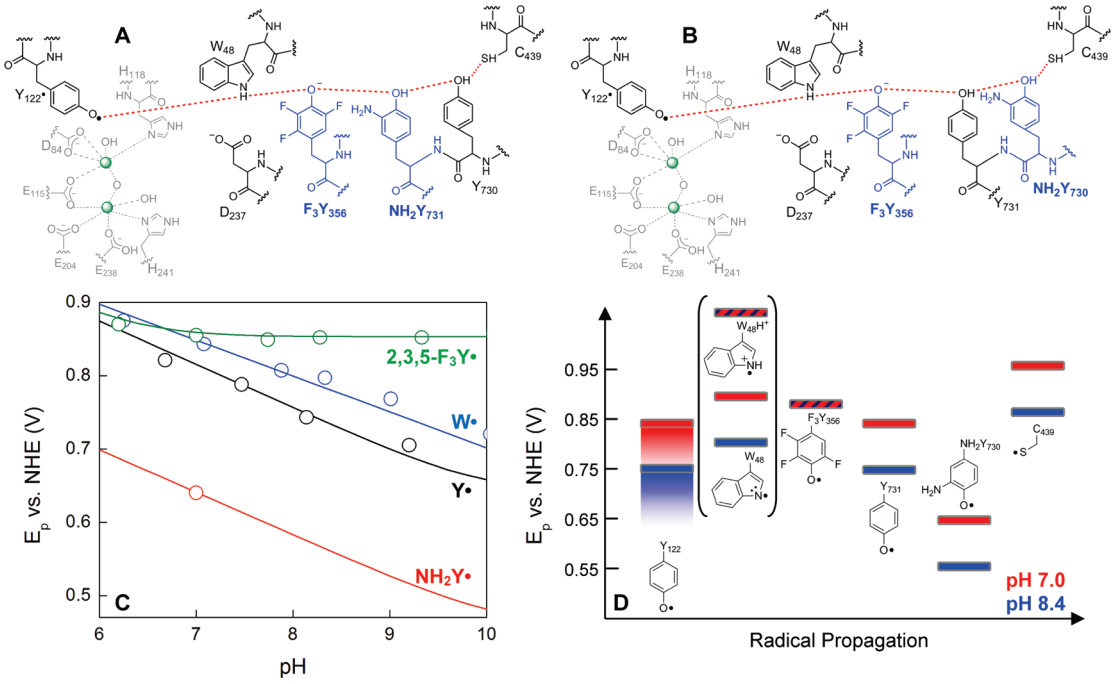

FIGURE 1: Proposed radical initiation pathway and its energetics in *E. coli* RNR with site-specific incorporation of unnatural amino acids (*13*). (A and B) Residues associated with the diferric cluster are colored gray, proposed pathway residues black (*13*), and the unnatural amino acids (F_3Y and NH_2Y) blue for probing the pathway in these studies. Note that the structural location of Y_{356} is unknown. (C) Peak potentials (E_p) for free (NH_2Y) and N-acetylated and C-amidated (Y, W, and F_3Y) amino acids, as a function of pH. The E_p values for $Y^\bullet$, $W^\bullet$, and 2,3,5-$F_3Y^\bullet$ have been previously determined (*25*), and the trace for $NH_2Y^\bullet$ has been generated from the reduction potential determined at pH 7, assuming Nernstian behavior (*27*). (D) The E_p values from panel C were assigned to residues in the radical propagation pathway to provide a qualitative energy landscape. Red and blue rectangles represent the peak potentials for each amino acid at pH 7.0 and 8.4, respectively. The peak potentials of $WH^{\bullet+}$ and $F_3Y^\bullet$ are represented by red rectangles with blue diagonal lines as they do not change between pH 7 and 8.4. The E_p range for $Y_{122}^\bullet$ is expanded (indicated by shading), because its properties relative to the other three Y residues, including its pK_a, are unique. $Y_{122}^\bullet$ has a half-life of ~4 days and likely represents a thermodynamic hole (*45*). Brackets are placed around W_{48} as no direct evidence that places it on the pathway is available. If it is on the pathway, its protonation state, $W_{48}H^{\bullet+}$ vs $W_{48}^\bullet$, that participates in radical transfer is unknown, and therefore, E_p values for both of these species are included.

phenolic pK_a values ranged from 5.6 to 8.4 and their E_p values varied from −50 to 270 mV relative to blocked Y in the physiological pH range (*25*). Perturbation of both of these properties could be mechanistically informative in studying PCET.

Expressed protein ligation (EPL) was used to incorporate F_nY analogues (where n = 1−4) (*18*, *25*, *26*) in place of Y_{356} in β2. To obtain sufficient amounts of semisynthetic β2 to conduct physical biochemical studies, two additional mutations, $V_{353}G$ and $S_{354}C$ in β2, were required. This double mutant, $V_{353}G/S_{354}C$-β2, at pH 7.6 had 25% of the activity of wt-β2. Henceforth, intein wt-β2 refers to $V_{353}G/S_{354}C$-β2 made by EPL.

The pH−rate profiles of F_nY_{356}-β2s with α2, CDP, and ATP were studied from pH 6.5 to 9.2, and the ability to produce dNDPs was compared to that of intein wt-β2 (*18*). Analysis of the rates of dNDP formation relative to intein wt-β2 versus the relative differences in the E_p of each F_nY relative to Y at each pH (Figure 1C) revealed three different activity regimes. In the first regime, where the E_p difference between F_nY and Y varied from −40 to 80 mV, the rate-limiting step in dNDP formation is a conformational change that precedes radical transfer. Intein wt-β2 and F_nY-β2s within this range are 100% active. In the second regime, where the E_p difference increased from 80 to 200 mV greater than that of Y, the specific activities of mutant RNRs decreased from 100% to a few percent. These data suggested that the rate-limiting step had changed from a conformational change to a step (or steps) in the radical propagation process. Finally, in the third regime, where the E_p difference was greater than 200 mV, no dNDPs are produced and the radical transfer process was shut down. If the interpretation of the pH−rate profiles of F_nY-β2s is correct, then it may be possible to detect transient intermediates during radical propagation in the second activity regime. Our studies suggested that F_3Y_{356}-β2 would be the most interesting F_nY-β2 to investigate in this regime.

The proposed pathway (Figure 1A,B) has been further explored via replacement of Y_{730} and Y_{731} in α2 with NH_2Y, a tyrosine analogue that is easier to oxidize than Y by 190 mV at pH 7 (Figure 1C). α in these studies has a single mutation, Y to NH_2Y (*19*). SF experiments in the presence of β2, CDP, and ATP revealed that an NH_2Y radical ($NH_2Y^\bullet$) is generated in a kinetically competent fashion in two phases with rate constants of 18 and 2.5 s^{-1} with NH_2Y_{731}-α2 and of 12 and 2.5 s^{-1} with NH_2Y_{730}-α2 at pH 7.6 (*19*). These studies and more recent studies (E. C. Minnihan, M. R. Seyedsayamdost, and J. Stubbe, manuscript in preparation) have further revealed that these mutants can make dNDPs at rates of 0.3−0.6 s^{-1}, substantially slower than the rates of formation of $NH_2Y^\bullet$.

In this paper, we examined F_3Y_{356}-β2 with α2, CDP, and ATP to look for radical intermediates by SF and RFQ EPR spectroscopy, and none were detected. The hypothesis that an E_p difference of >80 mV between F_3Y and Y changes the rate-determining step of RNR from conformational gating to a step or steps involved in PCET has also been examined: F_3Y-β2 was incubated with NH_2Y_{731}-α2 or NH_2Y_{730}-α2, and the pH−rate profile of formation of $NH_2Y^\bullet$ from pH 6.5 to 9.2 was investigated by SF absorption spectroscopy. The rate constants for $NH_2Y^\bullet$ formation are triphasic. Despite the kinetic complexity, they reveal that the pH−rate profile for $NH_2Y^\bullet$ formation is very

similar to that observed previously in the steady state for dNDP formation with F_3Y_{356}-β2, α2, CDP, and ATP and is distinct from the steady state data with the intein wt-β2 control. A kinetic model that accommodates these results and supports the proposed shift in the rate-limiting step is presented, and the kinetic simulations provide an explanation for why transient radical intermediates are not detected. This model provides a framework for future studies involving F_nY incorporation using evolved tRNA/tRNA synthetase pairs and addressing the importance of W_{48} in the pathway (Figure 1A,B).

MATERIALS AND METHODS

Materials. [2-^{14}C]CDP (50 μCi/mL) was purchased from Moravek Biochemicals, and calf intestine alkaline phosphatase (20 units/μL) was from Roche. Lithium 8-hydroxyquinoline-6-sulfonate and Sephadex G-25 were from Sigma. 2-(*N*-Morpholino)-ethanesulfonic acid (Mes), *N*-(2-hydroxyethyl)piperazine-*N*′-2-ethanesulfonic acid (Hepes), *N*-[tris(hydroxymethyl)methyl]-3-aminopropanesulfonic acid (Taps), 2-(cyclohexylamino)ethanesulfonic acid (Ches), and Emulsifier-Safe scintillation liquid were obtained from EMD Bioscience. Slide-a-lyzer cassettes were from Pierce. α2 was expressed, purified, and prereduced as reported and had a specific activity of 2500 nmol min^{-1} mg^{-1} (*18*, *28*). *E. coli* thioredoxin (TR, 40 units/mg) (*29*) and TR reductase (TRR, 1800 units/mg) were isolated as previously described (*30*). $Y_{730}NH_2Y$-α2 and $Y_{731}NH_2Y$-α2 were isolated as previously described and had specific activities of 100 and 175 nmol min^{-1} mg^{-1}, respectively (*19*).

Semisynthesis of F_3Y_{356}-β2. Generation of F_3Y_{356}-β2 by EPL and its purification were conducted as detailed previously (*31*).

Generation of Apo F_3Y_{356}-β2 with Lithium 8-Hydroxyquinoline-6-sulfonate. The apo form of intein wt-β2 and F_3Y_{356}-β2 were generated by a modification of the procedure of Atkin et al. (*32*). Briefly, a solution of 2.5 mL of each β2 variant ($\sim$20 mg, 90 μM) was dialyzed against 500 mL of chelator solution consisting of 1 M imidazole, 30 mM NH_2OH, and 50 mM 8-hydroxyquinoline-6-sulfonate (pH 7.0) in a 3 mL Slide-a-lyzer cassette for 3 h. The chelator was then removed by dialysis against 4 L of Hepes buffer [50 mM Hepes and 5% glycerol (pH 7.6)] for 3 h and further by being desalted on a Sephadex G-25 column (1.5 cm $\times$ 23 cm, 40 mL) equilibrated in Hepes buffer. This procedure gives the apo form of each β2 variant in 80−95% yield. The concentration of apo β2 was determined using an ε_{280} of 120 mM^{-1} cm^{-1}.

Reconstitution of Apo β2. The apo form of each β2 variant was reconstituted as reported previously. This procedure yields a radical content of $\sim$1.2 $Y_{122}^{\bullet}$/β2 as determined by the dropline method (*33*).

Spectrophotometric and Radioactive RNR Assays. RNR activity assays were performed as previously described (*18*). The final concentrations of α2 and β2 variants in these assays were 3 μM. The specific activity of [2-^{14}C]CDP was 3800 cpm/nmol.

Single-Wavelength and Diode Array SF Absorption Spectroscopy. SF absorption kinetics were performed on an Applied Photophysics DX.17MV instrument equipped with the Pro-Data upgrade. The temperature was maintained at 25 °C with a Lauda RE106 circulating water bath. Single-wavelength kinetics experiments utilized PMT detection at 410 nm (λ_{max} of $Y_{122}^{\bullet}$ with an ε of 3700 M^{-1} cm^{-1}) (*33*), 510 nm (λ_{max} of $W^{\bullet}$ with an ε of 2200 M^{-1} cm^{-1}), and 560 nm (λ_{max} of $WH^{\bullet+}$ with an ε of 3000 M^{-1} cm^{-1}) (*34*). Typically, prereduced α2 (50−70 μM) and ATP (6 mM) in one syringe were mixed with F_3Y_{356}-β2 (50−70 μM) and CDP (2 mM) in a 1:1 ratio in 50 mM Taps, 15 mM $MgSO_4$, and 1 mM EDTA (pH 8.4). Time courses shown are the average of at least five individual traces. Diode array SF absorption spectroscopy was conducted with an Applied Photophysics PDA.1 photodiode array detector. The concentrations of the reaction components were the same as described for single-wavelength kinetics.

RFQ EPR Spectroscopy. RFQ EPR samples were prepared using an Update Instruments 1019 Syringe Ram Unit, a model 715 Syringe Ram Controller, and a quenching bath. The temperature of the liquid isopentane bath was controlled with a Fluke 52 dual input thermometer, equipped with an Anritsu Cu thermocouple probe for the isopentane bath and the funnel. Stainless steel packers were purchased from McMaster-Carr and were cut to a length of 40 cm and deburred at the Massachusetts Institute of Technology machine shop. The dead time of the setup was determined to be 16 $\pm$ 2 ms with two independent measurements of the myoglobin−NaN_3 test reaction. A packing factor of 0.60 $\pm$ 0.05 was reproducibly obtained as tested with intein wt-β2 samples. Routinely, a ram push velocity of 1.25 or 1.6 cm/s was used and the displacement was adjusted to expel 300 μL of sample after the reaction.

Operation of the apparatus was similar to the procedure previously described (*35*). Typically, prereduced α2 (50−70 μM) and ATP (6 mM) in one syringe were mixed with F_3Y_{356}-β2 and CDP (2 mM) in the second syringe in a 1:1 ratio in 50 mM Taps, 15 mM $MgSO_4$, and 1 mM EDTA (pH 8.4). When the temperature of the EPR tube−funnel assembly had equilibrated to the bath temperature, the contents of each syringe were mixed rapidly in a mixing chamber and aged for a predetermined time period by pushing the contents through a reaction loop. The sample was sprayed into the EPR tube−funnel assembly that was held $\leq$1 cm from the spray nozzle. The assembly was immediately returned to the bath, and the crystals were allowed to settle for 15−30 s. The sample was then packed into the EPR tube using the stainless steel packers described above.

EPR spectra were recorded at the Department of Chemistry Instrumentation Facility on a Bruker ESP-300 X-band (9.4 GHz) spectrometer. Spectra at 77 K were recorded with a quartz finger dewar filled with liquid N_2; spectra at 15 K were recorded with an Oxford liquid helium cryostat and an Oxford ITC 503 temperature controller. Unless noted otherwise, EPR parameters were as follows: power, 50 μW; modulation amplitude, 1.5 G; modulation frequency, 100 kHz; time constant, 5.12 ms; and scan time, 41.9 s.

pH−Rate Profile of $NH_2Y^{\bullet}$ Formation in the Reaction of F_3Y_{356}-β2 with NH_2Y-α2s Monitored by SF Absorption Spectroscopy. NH_2Y-α2 was prepared and prereduced as detailed previously (*19*). In all experiments, prereduced NH_2Y-α2 and ATP were mixed with F_3Y_{356}-β2 and CDP, yielding final concentrations of 4 μM, 3 mM, 4 μM, and 1 mM, respectively. Single-wavelength kinetics were monitored using PMT detection at 320 nm (λ_{max} of $NH_2Y_{731}^{\bullet}$ with an ε of 11000 M^{-1} cm^{-1}) or 325 nm (λ_{max} of $NH_2Y_{730}^{\bullet}$ with an ε of 10500 M^{-1} cm^{-1}) (*19*). Reactions were conducted in 15 mM $MgSO_4$, 1 mM EDTA, and 50 mM Goods buffers [Mes (pH 6.5−7), Hepes (pH 7−8), Taps (pH 8−8.8), or Ches (pH 8.8−9.2) buffer] adjusted to the desired pH. Syringes and reaction lines were equilibrated in the desired buffer prior to the experiment. At each pH, six to eight traces were averaged and analyzed using OriginPro. Iterative rounds of fitting were conducted until the R^2 value was maximized ($\geq$0.99), and the residual plot was randomly scattered around zero $\pm$ $\leq$0.001 absorbance unit.

RESULTS

Pre-Steady State Experimental Design. Previous pre-steady state examination of wt RNR at pH 7.6 has shown that production of dCDP is limited in rate by a conformational change that precedes radical transfer, resulting in a burst of dCDP formation in the first turnover with rate constants of 4.4−10 s^{-1} (*36*). In wt RNR, this conformational change(s) kinetically masks detection of the proposed aromatic amino acid radical intermediates during radical transfer (Figure 1A,B). Thus, detection of transient radical intermediates requires, at a minimum, that the rate constant for radical transfer be diminished relative to that for the conformational step. Our previous results with F_nY-β2s suggested that insertion of F_3Y in place of Y_{356} provides a sufficient shift in the driving force for radical propagation, to make it rate-limiting at elevated pH (*18*). Thus, it is possible that pathway radical intermediates could be detected by RFQ EPR methods at elevated pH.

Increasing the $Y_{122}^{\bullet}$ Radical Content of Semisynthetic F_3Y_{356}-β2. To maximize our chances of detecting low levels of pathway radical intermediates, we focused on increasing the concentration of $Y_{122}^{\bullet}$ in the semisynthetic β2s using the method of Atkins et al. (*32*). With both intein wt-β2 and F_3Y_{356}-β2, we were able to obtain ~1.2 $Y_{122}^{\bullet}$/β2 with good protein recoveries (80−95%). The UV−vis spectrum, the EPR spectrum, and the SDS−PAGE results of these proteins are shown in Figures S1 and S2 of the Supporting Information. The spectra are identical to those of recombinant wt-β2, indicating an intact diferric $Y_{122}^{\bullet}$ cofactor. Assays for dCDP production before and after application of this procedure gave specific activities that correlated with $Y_{122}^{\bullet}$ content. Thus, the procedure increased the radical content of F_3Y-β2 and elevated nucleotide reduction activity proportionally.

SF Absorption and RFQ EPR Spectroscopies with F_3Y_{356}-β2 and α*2*. To test whether radical intermediates could be detected during the radical propagation process with F_3Y_{356}-β2 at pH 8.4, where this process is proposed to be rate-limiting, SF absorption and RFQ EPR studies were conducted with wt-α2. Using the E_p values measured for the blocked amino acids, W, F_3Y, Y, and NH_2Y (Figure 1C), an energy landscape for the pathway (Figure 1D) was created to help visualize how insertion of F_3Y into the pathway and pH might alter the ability of adjacent residues in the pathway to mediate its oxidation. If forward radical transfer is slow at pH 8.4, for example, then a neutral W_{48} could build up, if it is not rapidly reduced by Y_{122}. $W^{\bullet}$ radicals have reported λ_{max} values from 485 to 530 nm (ε = 1750−2300 M^{-1} cm^{-1}). We also considered the possibility that $WH^{\bullet+}$ might be observed, and they have reported λ_{max} values between 560 and 600 (ε = 2500−2900 M^{-1} cm^{-1}) (*34*, *37*). If reverse radical transfer is slow, then the species most likely to build up at pH 8.4 is $Y_{731}^{\bullet}$, based on the E_p difference of 110 mV relative to F_3Y (Figure 1C,D). $Y^{\bullet}$ radicals have λ_{max} values in the range of 407−410 (ε = 2750−3200 M^{-1} cm^{-1}) (*38*, *39*). The results from SF absorption experiments are presented in Figure 2A. They show that no changes are observed at 410 nm (λ_{max} for $Y_{122}^{\bullet}$), 510 nm, or 560 nm. The minor changes that are observed are likely related to small structural perturbations associated with the diiron cluster upon binding to α2 (*20*). SF diode array absorption spectroscopy also failed to reveal any changes in the region of 400−800 nm (data not shown). Under these experimental conditions, no absorption features associated with a $W^{\bullet}$ or $WH^{\bullet+}$ were apparent.

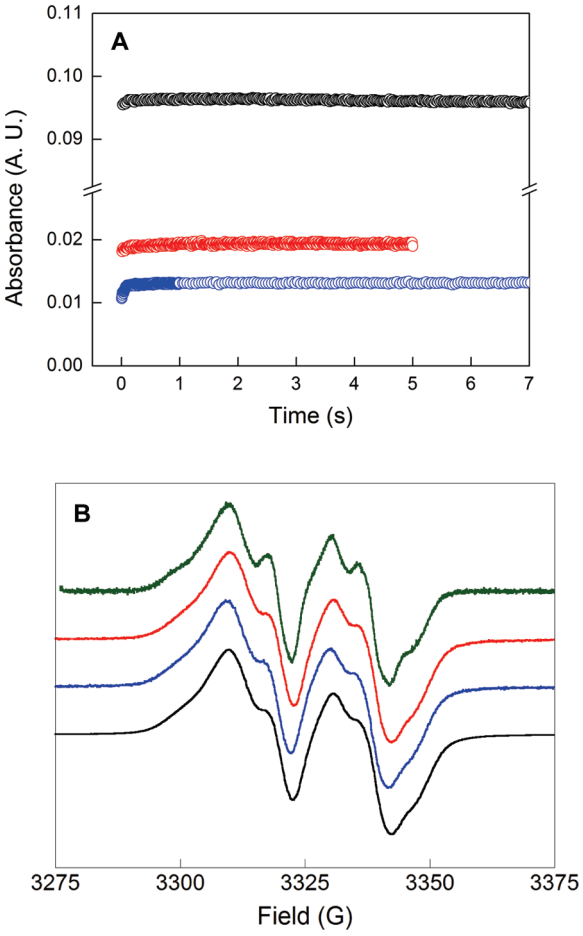

FIGURE 2: SF absorption and RFQ EPR spectroscopies with F_3Y_{356}-β2 in the presence of α2, CDP, and ATP at pH 8.4. (A) Single λ SF time courses monitored at 410 (black), 510 (red), and 560 nm (blue). (B) RFQ EPR spectra of samples quenched at 72 ms (black), 138 ms (blue), and 1.9 s (red) with the EPR spectrum recorded at 77 K. The EPR spectrum of the 1.9 s quench time point was recorded at 15 K (green).

As mentioned above, the absorption features associated with the $Y^{\bullet}$ range from 407 to 410 nm with varying degrees of sharpness. The $Y_{122}^{\bullet}$ and $Y_{731}^{\bullet}$ features are thus likely to be similar, making buildup of a transient $Y_{731}^{\bullet}$ difficult to distinguish from $Y_{122}^{\bullet}$ by visible spectroscopy. The EPR features of $Y_{122}^{\bullet}$ and $Y_{731}^{\bullet}$, on the other hand, are highly dependent on the dihedral angle of the β protons relative to the aromatic ring (*40*, *41*). On the basis of the crystal structures of α2 and β2, Y_{122}, Y_{731}, and Y_{730} have dihedral angles of ~90°, 33°, and 37°, respectively (*13*), making it feasible that the EPR spectra of the latter two would be distinct from that of $Y_{122}^{\bullet}$ (*42*). In accord with the structural data, we recently determined a dihedral angle of 46° for $NH_2Y_{730}^{\bullet}$ by EPR analysis (*43*). Consequently, RFQ EPR studies were conducted under conditions similar to those in the SF absorption experiments to look for a new $Y^{\bullet}$. The reaction was quenched from 28 to 1912 ms. The traces obtained at 72, 138, and 1912 ms are shown in Figure 2B and those at 28 and 612 ms in Figure S3 of the Supporting Information. EPR analysis and spin quantitation at 77 or 15 K at all time points showed that the $Y^{\bullet}$ concentration observed is identical to the $Y_{122}^{\bullet}$ concentration at time zero. The SF absorption and RFQ EPR spectroscopy experiments have thus failed to reveal formation of any pathway radical intermediates. We estimate that the lower limit of detection of $W^{\bullet}$ radicals by SF spectroscopy would be 1 μM,

~3% of the amount of protein. The lower limit for Y• detection by EPR methods is 1.5−3 μM and is estimated to be 5−10% of the protein. A rationalization for the lack of buildup of intermediates is presented below.

Use of NH_2Y-α2 as a Reporter of Forward Radical Transfer with F_3Y_{356}-β2. Our previous SF studies at pH 7.6 with β2, NH_2Y_{731}-α2 (or NH_2Y_{730}-α2), CDP, and ATP revealed that $NH_2Y^•$ is formed with biphasic kinetics and rate constants of 18 and 2.5 s^{-1} (12 and 2.5 s^{-1}) (*19*). The faster rate constants were proposed to be associated with electron delocalization within the protein in a nonproductive conformation for nucleotide reduction, with $NH_2Y^•$ formation resulting because of the ease of its oxidation. The slower rate constants were proposed to be associated with the rate-limiting conformational change responsible for dNDP production under steady state conditions. $NH_2Y^•$ formation was "complete" within 20 s, and its concentration remained unchanged for several minutes. The decay of $NH_2Y^•$ is slow with a rate constant of 0.0062 ± 0.0012 for $NH_2Y_{731}^•$ (Figure S4 of the Supporting Information) and 0.0043 ± 0.0011 s^{-1} for $NH_2Y_{730}^•$ (Figure S5 of the Supporting Information). Finally, both position 730 and 731 NH_2Y mutants supported dCDP formation with rate constants of 0.3−0.6 s^{-1}, substantially lower than the rate constant of NH_2Y• production (E. C. Minnihan, M. R. Seyedsayamdost, and J. Stubbe, manuscript in preparation). These rate constants would be further reduced with F_3Y_{356}-β2, as intein wt-β2 has 25% of the activity of wt-β2. These observations together suggest that under the conditions of the SF experiments described subsequently, NH_2Y can function as a radical trap reporting on the rate constant for forward radical propagation.

SF Absorption Spectroscopy with F_3Y_{356}-β2, NH_2Y-α2, CDP, and ATP. SF experiments were thus conducted with F_3Y_{356}-β2 and NH_2Y_{730}-α2 or NH_2Y_{731}-α2. The final concentration of protein in these experiments was 4 μM, similar to those previously reported in the steady state pH−rate profile studies (3 μM) (*18*, *36*). The ability to generate 1.2 $Y_{122}^•$ per $Y_{356}F_3Y$-β2 greatly facilitated the analysis.

The results of the pH-dependent SF experiments with NH_2Y_{730}-α2 (or NH_2Y_{731}-α2) and F_3Y_{356}-β2 are shown in Figure 3. Expanded views of the first several seconds of each trace are shown in Figure S6 of the Supporting Information (for $Y_{731}NH_2Y$-α2) and Figure S7 of the Supporting Information (for $Y_{730}NH_2Y$-α2). Reactions monitored for 20 s at pH 6.5, 8.45, and 8.6 (for $Y_{731}NH_2Y$-α2) and at pH 8.65 (for $Y_{730}NH_2Y$-α2) are shown in Figure S8 of the Supporting Information. The kinetic parameters are summarized in Table 1.

Fits to the kinetic traces in all cases required three exponentials. These results contrast to those with wt-β2 and NH_2Y-α2, which generate a $NH_2Y^•$ with all substrate−effector pairs in two kinetic phases. The molecular basis for the different phases is not understood, but our interpretation is that the slowest kinetic phase is associated with dCDP formation as observed in the steady state pH−rate profile studies with F_3Y_{356}-β2, wt-α2, CDP, and ATP (*18*). The second kinetic phase may be associated with the mutations ($V_{353}G$ and $S_{354}C$) that, as noted above, are required for efficient semisynthesis of β2. We propose that these two residues, likely located at the α2−β2 interface, generate an additional conformation that binds α2 and results in $NH_2Y^•$ formation, and that the fastest phase is associated with nonproductive conformational changes, as noted above. Three kinetic phases have previously been observed for the data associated with formation of 3-hydroxytyrosine radical (DOPA•) from DOPA-β2, α2, CDP, and ATP, also made by the EPL method (*17*). The analysis of these pH profiles presented below focuses mainly on the slowest, third kinetic phase, as it corresponds to dCDP production in the steady state.

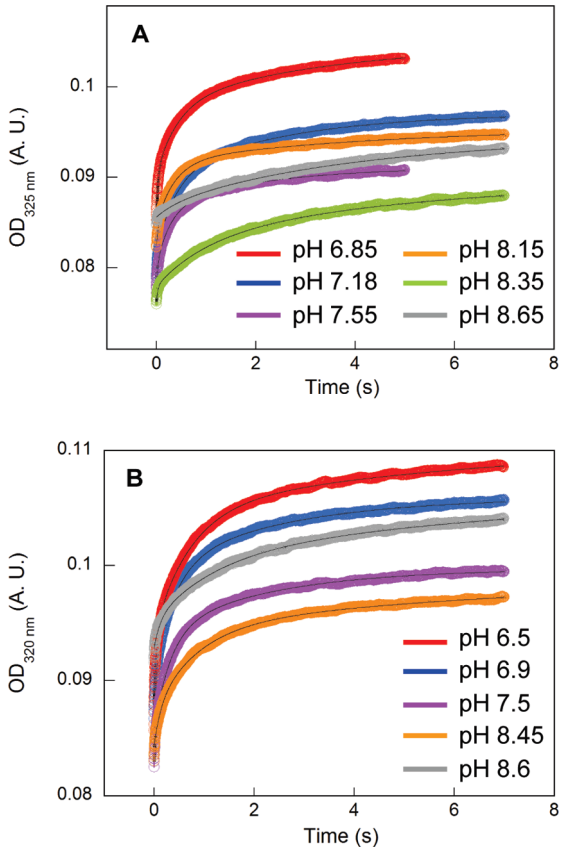

FIGURE 3: SF absorption spectroscopy of NH_2Y-α2s, F_3Y_{356}-β2, CDP, and ATP as a function of pH. Reaction of F_3Y_{356}-β2 with NH_2Y_{730}-α2 (A) or NH_2Y_{731}-α2 (B). Each trace is an average of six to eight traces. Black lines describe triexponential fits to the data. See Table 1 for kinetic parameters.

Analysis of the pH−Rate Profile for $NH_2Y^•$ Formation with F_3Y_{356}-β2 and NH_2Y-α2. The pH dependence of wt RNR activity is not understood but is associated with conformational changes and not chemistry. Here, pH is used to modulate the driving force for radical transfer (Figure 1C,D) based on our previously observed correlation between the rate of dNDP formation and the E_p difference between F_3Y and Y between pH 7.8 and 8.7. To analyze the results in Figure 3, we plotted the rate constants for $NH_2Y^•$ formation as a function of pH for each kinetic phase (Figure 4A−C).

The data from the fastest phase with NH_2Y_{730}-α2 (Figure 4A, blue circles) and NH_2Y_{731}-α2 (Figure 4A, red circles) exhibited k_{obs} values that vary from 2.7 to 48.9 s^{-1} and from 7.8 to 26.2 s^{-1}, respectively. The amplitudes in this phase account for the smallest amount, 10−26%, of the total $NH_2Y^•$. Furthermore, unlike the other phases, the profile for NH_2Y_{731}-α2 is distinct from that for NH_2Y_{730}-α2 (Figure 4A and Figure S9 of the Supporting Information). The second kinetic phase exhibits rate constants from 0.38 to 3.8 s^{-1} (0.80 to 3.0 s^{-1}) with amplitudes of 37−50% of the total absorbance change (Figure 4B, blue circles and red circles), while the k_{obs} values for the third kinetic phase vary from 0.11 to 0.52 s^{-1} (0.09 to 0.42 s^{-1}) with amplitudes of 27−52% of the overall change (Figure 4C, blue circles and red circles). The profiles of the two slow kinetic phases have shapes very similar to that observed for dCDP formation with F_3Y-β2.

Table 1: Summary of the Kinetic Parameters for $NH_2Y^\bullet$ Formation in the Reaction of NH_2Y_{730}-α2 or NH_2Y_{731}-α2 with F_3Y_{356}-β2, CDP, and ATP

	first phase		second phase		third phase	
pH	k_{obs} (s^{-1})[a]	Amp[b] (% $Y_{122}^\bullet$)	k_{obs} (s^{-1})[a]	Amp[b] (% $Y_{122}^\bullet$)	k_{obs} (s^{-1})[a]	Amp[b] (% $Y_{122}^\bullet$)
			NH_2Y_{730}-α2			
6.85	30.8 ± 3.7	10 ± 1	2.4 ± 0.3	15 ± 2	0.31 ± 0.04	13 ± 2
7.18	41.7 ± 5.0	7 ± 1	2.7 ± 0.3	16 ± 2	0.42 ± 0.05	15 ± 2
7.55	48.9 ± 5.9	6 ± 1	3.8 ± 0.5	12 ± 1	0.52 ± 0.06	10 ± 1
8.15	21.8 ± 2.6	5 ± 1	2.8 ± 0.3	13 ± 2	0.23 ± 0.03	8 ± 1
8.35	32.9 ± 3.9	3 ± 1	1.0 ± 0.1	10 ± 1	0.20 ± 0.02	14 ± 2
8.65	2.7 ± 0.3	2 ± 1	0.38 ± 0.05	9 ± 1	0.11 ± 0.01	9 ± 2
			NH_2Y_{731}-α2			
6.5	24.7 ± 3.0	11 ± 1	1.7 ± 0.2	20 ± 2	0.21 ± 0.03	13 ± 2
6.9	26.2 ± 3.1	6 ± 1	2.5 ± 0.3	18 ± 2	0.40 ± 0.05	12 ± 1
7.5	28.6 ± 3.4	6 ± 1	3.0 ± 0.4	17 ± 2	0.44 ± 0.05	11 ± 1
8.45	7.8 ± 1.0	6 ± 1	1.2 ± 0.1	14 ± 2	0.12 ± 0.02	9 ± 1
8.6	8.3 ± 1.0	5 ± 1	0.80 ± 0.1	12 ± 1	0.09 ± 0.02	13 ± 2
9.2	–	–	–	–	–	–

[a]Estimated errors based on systematic factors. [b]The amount of $NH_2Y^\bullet$ trapped has been reported as a percentage of the total initial $Y_{122}^\bullet$, which in these experiments was 4.8 μM.

Our hypothesis is that the slowest kinetic phase is associated with the RNR conformation active in turnover. To analyze this phase further, the rate constants for $NH_2Y^\bullet$ formation with position 730 and 731 mutants were overlaid with those for dCDP formation in the steady state (Figure 4D). Also included is the profile for dCDP formation with intein wt-β2 (green squares). A direct comparison between the rate constants for pre-steady state $NH_2Y^\bullet$ formation and steady state dCDP formation (by F_3Y_{356}-β2 and α2) as a function of pH shows remarkable agreement. They overlap in all three activity regimes and are distinct from that of intein wt-β2 at pH >7.8 (Figure 4D, green squares). Because $NH_2Y^\bullet$ formation serves as a readout for forward radical transfer, the results indicate that a step in this process has the same pH-dependent rate constants as k_{cat} measured by steady state kinetic assays. This observation supports our original proposal that at high pH, the rate-determining step has shifted from a physical step to radical transfer and suggests that insertion of F_3Y results in a decrease in the rate constant for forward radical transfer as the reaction pH is increased.

DISCUSSION

Kinetic Simulations. To address our inability to detect radical intermediates with F_3Y_{356}-β2, despite an apparent shift in the rate-determining step, we conducted kinetic simulation studies. Figure 1D will be used as a means to predict the potential buildup of intermediates associated with insertion of F_3Y into the pathway. This energy landscape model of the pathway assumes that the reduction potentials and pK_a values of the residues involved are minimally perturbed by the protein environment. For residues Y_{356} in β2 and Y_{730} and Y_{731} in α2, these assumptions are supported by our recent studies in which 3-nitrotyrosine (NO_2Y) has been site-specifically incorporated into each of these positions (*44*, *45*). The model suggests that during forward PCET, the step most likely to be rate-limiting at pH 8.4 would be the oxidation of F_3Y by $W_{48}^\bullet$ based on E_p values of 0.85 and 0.8 V, respectively (Figure 1C,D). In the reverse direction at pH 8.4, the slowest step would be the oxidation of F_3Y by $Y_{731}^\bullet$, consistent with E_p values of 0.85 and 0.74 V, respectively (Figure 1C,D). Note that wt-α2 is used in these simulations.

The kinetic model in Figure 5 is based on our previous kinetic model for wt RNR at pH 7.6 and the data and simulations reported herein (*36*). Two points should be reiterated prior to presentation of the model. The first is that intein wt-β2 has 25% of the activity of wt-β2 because of the two additional mutations. Thus, the rate constants associated with the conformational change(s) used in the model could be elevated 4-fold for the wt RNR. The second is that while W_{48} has been incorporated into the original pathway model (*13*) and all subsequent renditions of this model (*15*, *24*, *46*), there is currently no direct evidence for its involvement in contrast with the proposed Y pathway residues. While in our model we have incorporated this residue, we and others are actively trying to address its involvement using multiple methods (*45*, *46*).

In the model in Figure 5, binding of CDP and effector ATP, step A, is followed by the rate-limiting conformational change, step B, that gates radical transfer. Subsequent to this change, $Y_{122}^\bullet$ is reduced and gives rise to $W_{48}^\bullet$, step C, which then generates $C_{439}^\bullet$ via F_3Y_{356}, Y_{731}, and Y_{730} transient radical intermediates, step D. One hopping step within step D, oxidation of F_3Y by $W_{48}^\bullet$, is proposed to be the rate-limiting step in the forward direction. $C_{439}^\bullet$ catalyzes nucleotide reduction, step E, which then gives rise to $Y_{731}^\bullet$ through a transient $Y_{730}^\bullet$ intermediate, step F. $Y_{731}^\bullet$ then regenerates $Y_{122}^\bullet$ via F_3Y_{356} and W_{48}, step G; this step could represent the rate-limiting step in reverse radical transfer. Dissociation of dCDP, step H, completes the catalytic cycle, although in the steady state the active site disulfide needs to be re-reduced for multiple turnovers to occur. In this model, the K_d values and rate constants colored black (steps A, E, F, and H) have been determined experimentally (*45*, *47*, *48*). Rate constants of 107 s^{-1} for dCDP formation, step E, and 100 s^{-1} for $Y_{356}^\bullet$ formation, step F, have been recently determined in studies using NO_2Y site-specifically incorporated in place of Y_{122} (NO_2Y_{122}-β2) (*45*). This protein does not have the additional mutations of the EPL-generated protein. A $NO_2Y^\bullet$ radical is transiently generated at position 122, which uncouples proton and electron transfer and unmasks, for the first time, the rate constant for dCDP formation and $Y_{356}^\bullet$ formation in the reverse direction. The rate constants colored gray (steps C and F and k_{rev} in step B) were used in our

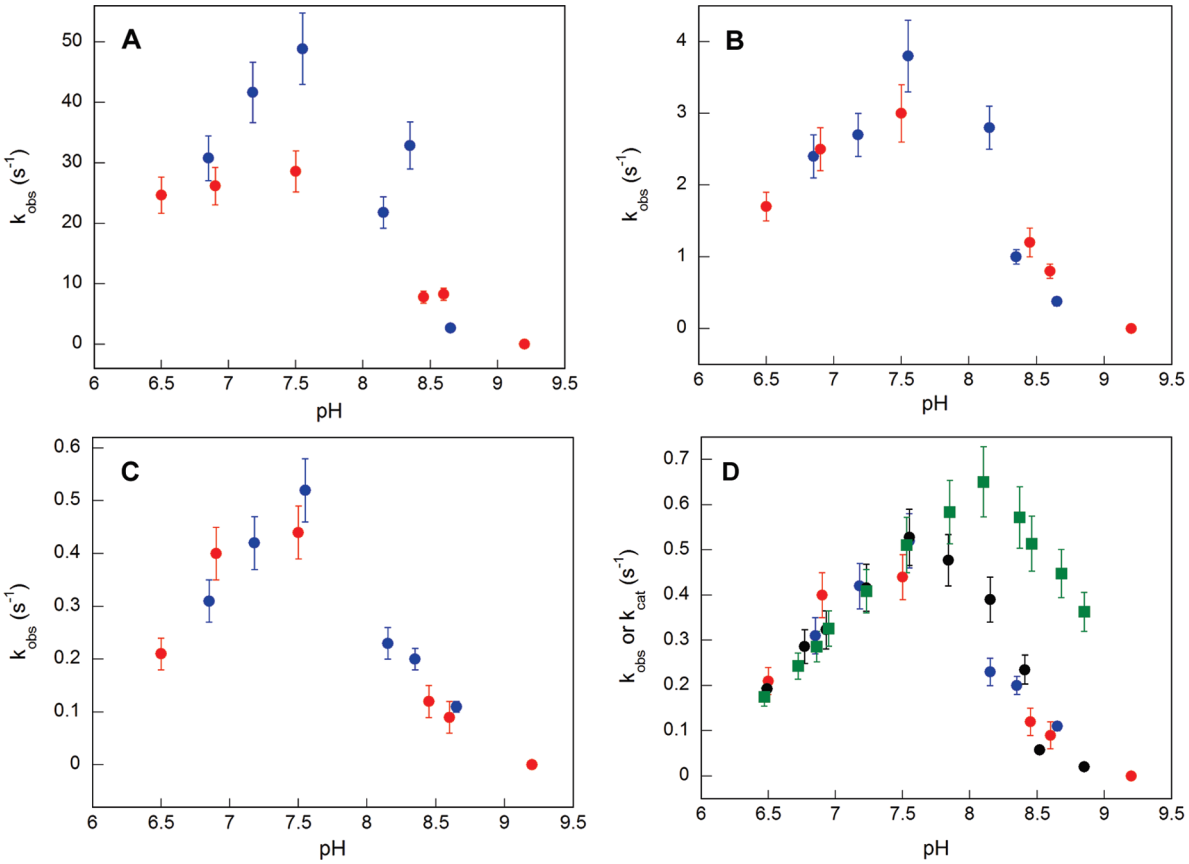

FIGURE 4: pH−rate profiles for $NH_2Y^{\bullet}$ formation in the reactions of NH_2Y_{730}-α2 (blue circles) or NH_2Y_{731}-α2 (red circles) with F_3Y_{356}-β2 in the presence of CDP and ATP. pH dependence of the rate constants from the first (A), second (B), and third (C) kinetic phases determined from the triexponential fits (Table 1). In panel D, the data from panel C are overlaid with the pH−rate profiles for [^{14}C]dCDP formation with F_3Y_{356}-β2 and wt α2 (black circles) and with intein wt-β2 and wt α2 (green squares), determined in a previous study (*18*).

original kinetic model for wt RNR (pH 7.6) to reproduce our inability to observe the disappearance and reappearance of $Y_{122}^{\bullet}$ or to detect any radical intermediates under a wide range of conditions (*36*). The rate constants colored red (k_{fwd} in steps B, D, and G) have been determined experimentally herein and assigned to these steps as described subsequently. Note that the rate constant associated with step B (0.5 s^{-1}) might be elevated 4-fold as described above. The rate constants colored blue have been simulated herein.

We began this exercise by simulating the effect of a solely rate-limiting reverse radical transfer. In this case, step D and the intermediate preceding it were eliminated from the model, and we assigned to step G the k_{obs} of 0.2 s^{-1}, obtained at pH ~8.4 with NH_2Y_{730}-α2 by SF absorption spectroscopy for $NH_2Y^{\bullet}$ formation (see Table 1). This assignment is consistent with E_p differences between F_3Y and Y at pH 8.4 described above (*25*). The simulations show that with 20 μM RNR, the $Y_{731}^{\bullet}$ concentration would increase to >12.5−14 μM. The RFQ EPR studies, however, failed to detect any new $Y^{\bullet}$. Changing the parameters for step C (100−300 s^{-1} for k_{rev}) or step G (1−100 s^{-1} for k_{rev}) still yielded >12 μM $Y_{731}^{\bullet}$. Thus, within the current kinetic framework, and the caveat that the pathway $Y^{\bullet}$s would be distinguishable from $Y_{122}^{\bullet}$, reverse radical transfer is not solely rate-limiting, consistent with our SF absorption studies in which NH_2Y-α2 serves as a reporter for forward radical transfer.

We next assumed a solely rate-limiting forward radical transfer. In this case, step G and the intermediate preceding it were eliminated from the model (Figure 5) and the slow step of 0.2 s^{-1} at pH ~8.4 (see Table 1) was applied to step D, consistent with E_p difference between W and F_3Y (Figure 1C,D). The kinetic simulations show that, at 20 μM RNR, $W_{48}^{\bullet}$ accumulates, reaching a concentration of 0.5−1.4 μM (using rates of 10^2−10^3 s^{-1} for step F and 300 s^{-1} for k_{rev} of step C). As discussed above, these concentrations are at or below our lower limit of detection. In addition, given the half-site reactivity for RNRs that we have observed in many of our experiments (*17*, *19*), the actual concentration of the radical would be even lower (0.25−0.7 μM). The k_{rev} for step C had to be increased to ≥300 s^{-1} relative to that of our original kinetic model for RNR (200 s^{-1}) to reproduce our inability to detect intermediates. This suggests an increased flux toward $Y_{122}^{\bullet}$ re-formation when F_3Y_{356} replaces Y_{356}. The faster the k_{rev} for step B or C, the smaller the amount of $W_{48}^{\bullet}$ that would build up. This simulation makes it much less likely that a $W_{48}H^{\bullet+}$ species is involved, vs a neutral $W^{\bullet}$, during forward PCET (Figure 1C,D; see below).

Finally, we assumed that forward and reverse radical transfers are both partially rate-limiting and assign steps D and G both to 0.2 s^{-1}. In this case, the simulations show that $Y_{731}^{\bullet}$ and $W_{48}^{\bullet}$ concentrations would reach <0.8 and 0.25−0.7 μM (after accounting for half-site reactivity), respectively. Thus, within the framework of the current model, rate-limiting forward or partially rate-limiting forward and reverse PCET are consistent with the inability to observe intermediates despite an apparent change in the rate-limiting step as a result of insertion of F_3Y into the pathway. This model serves as a starting point for examining the kinetics of F_3Y_{356}-β2 further, for example, by using rapid chemical quench methodology to examine the rate of dCDP formation.

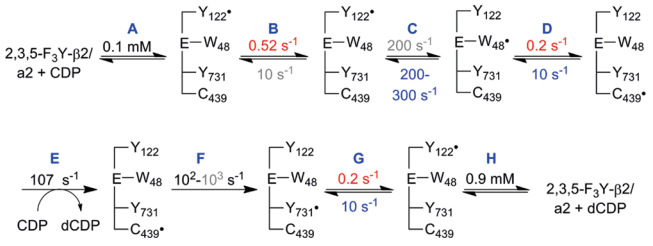

FIGURE 5: Kinetic model for the catalytic cycle of F_3Y_{356}-β2 with wt α2, CDP, and ATP, which have been omitted for clarity. The K_d values and the rate constants colored black have been measured experimentally (*45*, *47*, *48*); the rate constants colored gray have been adapted from our previous simulations (*36*), and those colored red have been measured herein and assigned to steps B, D, and G as described in the text. Rate constants colored blue have been simulated herein. When assuming rate-limiting reverse PCET, step D and the intermediate prior to D were eliminated from the model, and the k_{obs} of 0.2 s^{-1} was assigned to step G. When assuming a rate-limiting forward PCET, step G and the intermediate prior to G were eliminated from the model and the k_{obs} of 0.2 s^{-1} was assigned to step D. The k_{rev} values of steps C, D, and G have been assigned 200−300, 10, and 10 s^{-1}, respectively, to reproduce the lack of observable intermediates (i.e., $W_{48}^{\bullet}$).

The two models make different predictions about the lag phases in dCDP production. Evolution of a tRNA−tRNA synthetase pair for incorporation of F_3Y is in progress. These studies should remove the kinetic complexity associated with the two additional mutations required by the EPL method, increase the overall activity 4-fold, and simplify further analysis.

Implications for Radical Propagation. Despite the shift in the rate-determining step associated with the redox properties of F_3Y relative to W_{48} or Y_{731} (Figure 1C,D), no pathway intermediates are detectable. A modeling exercise incorporating recent kinetic parameters from studies with Y_{122} replaced with NO_2Y provides insight into why this might be the case and, if W_{48} is on the pathway, why a $W^{\bullet}$ radical and not a $WH^{\bullet+}$ radical is the most likely intermediate between Y_{122} and residue 356. We consider the $WH^{\bullet+}$ radical less likely given the following argument. If we assume the pK_a of F_3Y is minimally perturbed (*44*) and that a $WH^{\bullet+}$ radical participates in the pathway, the E_p difference between $WH^{\bullet+}$ and F_3Y would not change between pH 7 and 8.4 (Figure 1C). Our data indicate that the rate-determining step occurs between $Y_{122}^{\bullet}$ reduction and NH_2Y oxidation. Therefore, the rate-limiting step would be associated with oxidation of W_{48} by $Y_{122}^{\bullet}$ [oxidation of F_3Y by $WH^{\bullet+}$ is pH-independent, and that of Y_{731} by $F_3Y^{\bullet}$ is thermodynamically favored (Figure 1D)]. This conclusion is inconsistent with the observation that when F_nYs are placed at position 356, their pH−rate profiles differ from that of intein wt-β2. They would be the same if $Y_{122}^{\bullet}$-mediated W oxidation was slow. It is also inconsistent with the >200 mV E_p difference (in Figure 1D, Y_{122} is special and appears to be a thermodynamic hole) at pH 7 and a >310 mV difference at pH 8.4 between Y_{122} and $WH^{\bullet+}$. With $W_{48}^{\bullet}$ as an intermediate, on the other hand, an explanation for the change in the rate-determining step when F_3Y is inserted into the pathway becomes apparent. In the case of the neutral $W^{\bullet}$ radical, the E_p gap between Y_{122} and W_{48} does not change as a function of pH, $F_3Y^{\bullet}$-mediated oxidation of Y or NH_2Y is thermodynamically very favorable (Figure 1D), and thus oxidation of F_3Y by $W_{48}^{\bullet}$ remains as the basis for the observed changes. Between pH 7 and 8.4 (Figure 1C), the reaction becomes less favorable by 70 mV.

Our previous studies have demonstrated the importance of a $WH^{\bullet+}$ in active metallo-cofactor assembly and more specifically Y_{122} oxidation . In this case, the reaction is irreversible, and the "hot" Fe^{4+}/Fe^{3+} or $WH^{\bullet+}$ oxidants can drive the reaction toward $Y^{\bullet}$. In contrast, the PCET pathway must function reversibly. These studies and our other studies suggest that Nature has chosen W and Y as reversible redox conduits over long distances as the direction of radical hopping may be determined by the nature of the proton transfer reaction, and because their reduction potentials require minimal perturbation. W and Y contrast with many metal or organic cofactors (flavins and hemes) used by enzymes in which the protein environment must modulate the reduction potentials by >500 mV for the cofactor to function (*51*, *52*). W and Y have the appropriate chemical properties for fine-tuning the unusual radical propagation pathway in RNR.

The kinetic modeling provides a framework for thinking about optimal unnatural amino acids, for perturbing the pathway, for detecting intermediates, and for studying the PCET process at each step. For example, the model suggests that to detect intermediates in the pathway, a hot oxidant needs to replace $Y_{122}^{\bullet}$. Rapid reduction of the hot oxidant would lead to rapid production of pathway intermediates that would be unable to reoxidize the reduced form of the oxidant, allowing buildup an intermediate(s). This approach has recently been shown to be successful via placement of NO_2Y at position 122 that can be oxidized by the Fe^{4+}/Fe^{3+} radical but cannot be reoxidized by pathway radicals (*45*). The studies further suggest that NH_2Y substitution will be useful in examining the individual hopping steps of the three transiently involved $Y^{\bullet}$s in the pathway.

ACKNOWLEDGMENT

We thank Ellen C. Minnhan for helpful discussions.

SUPPORTING INFORMATION AVAILABLE

SDS−PAGE, UV−vis, and EPR characterization of the diferric $Y_{122}^{\bullet}$ cluster in semisynthetic F_3Y_{356}-β2 after its radical content had been increased (Figures S1 and S2); RFQ EPR traces of additional time points in the reaction of F_3Y_{356}-β2 with wt α2, CDP, and ATP (Figure S3); stability of $NH_2Y_{731}^{\bullet}$ and $NH_2Y_{730}^{\bullet}$ monitored by UV−vis and EPR spectroscopies (Figures S4 and S5); magnified views of SF UV−vis traces in the reaction of F_3Y_{356}-β2 with NH_2Y_{731}-α2 or NH_2Y_{730}-α2 (Figures S6−S8); and comparison of the pH profiles of high k_{obs} values for $NH_2Y^{\bullet}$ formation (Figure S9). This material is available free of charge via the Internet at http://pubs.acs.org.

REFERENCES

1. Stubbe, J., and van der Donk, W. A. (1998) Protein radicals in enzyme catalysis. *Chem. Rev. 98*, 705–762.
2. Jordan, A., and Reichard, P. (1998) Ribonucleotide reductases. *Annu. Rev. Biochem. 67*, 71–98.
3. Brown, N. C., and Reichard, P. (1969) Ribonucleoside diphosphate reductase. Formation of active and inactive complexes of proteins B1 and B2. *J. Mol. Biol. 46*, 25–38.
4. Thelander, L. (1973) Physicochemical characterization of ribonucleoside diphosphate reductase from *Escherichia coli*. *J. Biol. Chem. 248*, 4591–4601.
5. Wang, J., Lohman, G. J., and Stubbe, J. (2007) Enhanced subunit interactions with gemcitabine-5′-diphosphate inhibit ribonucleotide reductases. *Proc. Natl. Acad. Sci. U.S.A. 104*, 14324–14329.
6. Stubbe, J. (1990) Ribonucleotide reductases: Amazing and confusing. *J. Biol. Chem. 265*, 5329–5332.
7. Stubbe, J. (1998) Ribonucleotide reductases in the twenty-first century. *Proc. Natl. Acad. Sci. U.S.A. 95*, 2723–2724.
8. Licht, S., Gerfen, G. G., and Stubbe, J. (1996) Thiyl radicals in ribonucleotide reductases. *Science 271*, 477–481.

9. Nordlund, P., and Reichard, P. (2006) Ribonucleotide reductases. *Annu. Rev. Biochem. 75*, 681–706.
10. Ehrenberg, A., and Reichard, P. (1972) Electron spin resonance of the iron-containing protein B2 from ribonucleotide reductase. *J. Biol. Chem. 247*, 3485–3488.
11. Sjöberg, B.-M., Reichard, P., Gräslund, A., and Ehrenberg, A. (1978) The tyrosine free radical in ribonucleotide reductase from *Escherichia coli*. *J. Biol. Chem. 253*, 6863–6865.
12. Stubbe, J., Nocera, D. G., Yee, C. S., and Chang, M. C. Y. (2003) Radical initiation in the class I ribonucleotide reductase: Long-range proton-coupled electron transfer? *Chem. Rev. 103*, 2167–2201.
13. Uhlin, U., and Eklund, H. (1994) Structure of ribonucleotide reductase protein R1. *Nature 370*, 533–539.
14. Climent, I., Sjöberg, B.-M., and Huang, C. Y. (1992) Site-directed mutagenesis and deletion of the carboxyl terminus of *Escherichia coli* ribonucleotide reductase protein R2. Effects on catalytic activity and subunit interaction. *Biochemistry 31*, 4801–4807.
15. Ekberg, M., Sahlin, M., Eriksson, M., and Sjöberg, B.-M. (1996) Two conserved tyrosine residues in protein R1 participate in an intermolecular electron transfer in ribonucleotide reductase. *J. Biol. Chem. 271*, 20655–20659.
16. Ekberg, M., Birgander, P., and Sjöberg, B.-M. (2003) In vivo assay for low-activity mutant forms of *Escherichia coli* ribonucleotide reductase. *J. Bacteriol. 185*, 1167–1173.
17. Seyedsayamdost, M. R., and Stubbe, J. (2006) Site-specific replacement of Y_{356} with 3,4-dihydroxyphenylalanine in the β_2 subunit of *E. coli* ribonucleotide reductase. *J. Am. Chem. Soc. 128*, 2522–2523.
18. Seyedsayamdost, M. R., Yee, C. S., Reece, S. Y., Nocera, D. G., and Stubbe, J. (2006) pH rate profiles of F_nY_{356}-R2s (n = 2, 3, 4) in *Escherichia coli* ribonucleotide reductase: Evidence that Y_{356} is a redox-active amino acid along the radical propagation pathway. *J. Am. Chem. Soc. 128*, 1562–1568.
19. Seyedsayamdost, M. R., Xie, J., Chan, C. T., Schultz, P. G., and Stubbe, J. (2007) Replacement of Y730 and Y731 in the α2 subunit of *Escherichia coli* ribonucleotide reductase with 3-aminotyrosine using an evolved suppressor tRNA/tRNA-synthetase pair. *J. Am. Chem. Soc. 129*, 15060–15071.
20. Minnihan, E. C., Seyedsayamdost, M. R., and Stubbe, J. (2009) Use of 3-aminotyrosine to examine the pathway dependence of radical propagation in *Escherichia coli* ribonucleotide reductase. *Biochemistry 48*, 12125–12132.
21. Seyedsayamdost, M. R., Chan, C. T., Mugnaini, V., Stubbe, J., and Bennati, M. (2007) PELDOR spectroscopy with DOPA-β2 and NH_2Y-α2s: Distance measurements between residues involved in the radical propagation pathway of *E. coli* ribonucleotide reductase. *J. Am. Chem. Soc. 129*, 15748–15749.
22. Tommos, C., Skalicky, J. J., Pilloud, D. L., Wand, A. J., and Dutton, P. L. (1999) *De novo* proteins as models of radical enzymes. *Biochemistry 38*, 9495–9507.
23. Reece, S. Y., Stubbe, J., and Nocera, D. G. (2005) pH dependence of charge transfer between tryptophan and tyrosine in dipeptides. *Biochim. Biophys. Acta 1706*, 232–238.
24. Reece, S. Y., Hodgkiss, J. M., Stubbe, J., and Nocera, D. G. (2006) Proton-coupled electron transfer: The mechanistic underpinning for radical transport and catalysis in biology. *Philos. Trans. R. Soc. London, Ser. B 361*, 1351–1364.
25. Seyedsayamdost, M. R., Reece, S. Y., Nocera, D. G., and Stubbe, J. (2006) Mono-, di-, tri-, and tetra-substituted fluorotyrosines: New probes for enzymes that use tyrosyl radicals in catalysis. *J. Am. Chem. Soc. 128*, 1569–1579.
26. Reece, S. Y., Seyedsayamdost, M. R., Stubbe, J., and Nocera, D. G. (2006) Electron transfer reactions of fluorotyrosyl radicals. *J. Am. Chem. Soc. 128*, 13654–13655.
27. DeFelippis, M. R., Murthy, C. P., Broitman, F., Weinraub, D., Faraggi, M., and Klapper, M. H. (1991) Electrochemical properties of tyrosine phenoxy and tryptophan indolyl radicals in peptides and amino acid analogs. *J. Phys. Chem. 95*, 3416–3419.
28. Salowe, S., Bollinger, J. M., Jr., Ator, M., and Stubbe, J. (1993) Alternative model for mechanism-based inhibition of *Escherichia coli* ribonucleotide reductase by 2′-azido-2′-deoxyuridine 5′-diphosphate. *Biochemistry 32*, 12749–12760.
29. Chivers, P. T., Prehoda, K. E., Volkman, B. F., Kim, B. M., Markley, J. L., and Raines, R. T. (1997) Microscopic p*K*a values of *Escherichia coli* thioredoxin. *Biochemistry 36*, 14985–14991.
30. Russel, M., and Model, P. (1985) Direct cloning of the trxB gene that encodes thioredoxin reductase. *J. Bacteriol. 163*, 238–242.
31. Yee, C. S., Seyedsayamdost, M. R., Chang, M. C. Y., Nocera, D. G., and Stubbe, J. (2003) Generation of the R2 subunit of ribonucleotide reductase by intein chemistry: Insertion of 3-nitrotyrosine at residue 356 as a probe of the radical initiation process. *Biochemistry 42*, 14541–14552.
32. Atkin, C. L., Thelander, L., Reichard, P., and Lang, G. (1973) Iron and free radical in ribonucleotide reductase. Exchange of iron and Mossbauer spectroscopy of the protein B2 subunit of the *Escherichia coli* enzyme. *J. Biol. Chem. 248*, 7464–7472.
33. Bollinger, J. M., Jr., Tong, W. H., Ravi, N., Huynh, B. H., Edmondson, D. E., and Stubbe, J. (1995) Use of rapid kinetics methods to study the assembly of the diferric-tyrosyl radical cofactor of *E. coli* ribonucleotide reductase. *Methods Enzymol. 258*, 278–303.
34. Aubert, C., Vos, M. H., Mathis, P., Eker, A. P., and Brettel, K. (2000) Intraprotein radical transfer during photoactivation of DNA photolyase. *Nature 405*, 586–590.
35. Ballou, D. P. (1978) Freeze-quench and chemical-quench techniques. *Methods Enzymol. 54*, 85–93.
36. Ge, J., Yu, G., Ator, M. A., and Stubbe, J. (2003) Pre-steady-state and steady-state kinetic analysis of *E. coli* class I ribonucleotide reductase. *Biochemistry 42*, 10071–10083.
37. Baugher, J. F., and Grossweiner, L. I. (1977) Photolysis mechanism of aqueous tryptophan. *J. Phys. Chem. 81*, 1349–1354.
38. Feitelson, J., and Hayon, E. (1973) Electron ejection and electron capture by phenolic compounds. *J. Phys. Chem. 77*, 10–15.
39. Bansal, K. M., and Fessenden, R. W. (1976) Pulse radiolysis studies of the oxidation of phenols by $^{\bullet}SO_4^-$ and Br_2^- in aqueous solutions. *Radiat. Res. 67*, 1–8.
40. Pesavento, R. P., and van der Donk, W. A. (2001) Tyrosyl radical cofactors. *Adv. Protein Chem. 58*, 317–385.
41. Lendzian, F. (2005) Structure and interactions of amino acid radicals in class I ribonucleotide reductase studied by ENDOR and high-field EPR spectroscopy. *Biochim. Biophys. Acta 1707*, 67–90.
42. Svistunenko, D. A., and Cooper, C. E. (2004) A new method of identifying the site of tyrosyl radicals in proteins. *Biochem. J. 87*, 582–595.
43. Seyedsayamdost, M. R., Argirevic, T., Minnihan, E. C., Stubbe, J., and Bennati, M. (2009) Structural examination of the transient 3-aminotyrosyl radical on the PCET pathway of *E. coli* ribonucleotide reductase by multifrequency EPR spectroscopy. *J. Am. Chem. Soc. 131*, 15729–15738.
44. Yokoyama, K., Uhlin, U., and Stubbe, J. (2010) Site-specific incorporation of 3-nitrotyrosine as a probe of pKa perturbation of redox-active tyrosines in ribonucleotide reductase. *J. Am. Chem. Soc. 132*, 8385–8397.
45. Yokoyama, K., Uhlin, U., and Stubbe, J. (2010) A hot oxidant, 3-NO_2Y122 radical, unmasks conformational gating in ribonucleotide reductase. *J. Am. Chem. Soc. 132*, 15368–15379.
46. Jiang, W., Xie, J., Varano, P. T., Krebs, C., and Bollinger, J. M. (2010) Two distinct mechanisms of inactivation of the class Ic ribonucleotide reductase from *Chlamydia trachomatis* by hydroxyurea: Implications for the protein gating of intersubunit electron transfer. *Biochemistry 49*, 5340–5349.
47. van Döbeln, U., and Reichard, P. (1976) Binding of substrates to *Escherichia coli* ribonucleotide reductase. *J. Biol. Chem. 253*, 3616–3622.
48. Allard, P., Kuprin, S., Shen, B., and Ehrenberg, A. (1992) Binding of the competitive inhibitor dCDP to ribonucleoside-diphosphate reductase from *Escherichia coli* studied by ^{1}H NMR. Different properties of the large protein subunit and the holoenzyme. *Eur. J. Biochem. 280*, 635–642.
49. Bollinger, J. M., Jr., Tong, W. H., Ravi, N., Huynh, B. H., Edmondson, D. E., and Stubbe, J. (1994) Mechanism of assembly of the tyrosyl radical-diiron(III) cofactor of *E. coli* ribonucleotide reductase. 3. Kinetics of the limiting Fe^{2+} reaction by optical, EPR, and Mossbauer spectroscopies. *J. Am. Chem. Soc. 116*, 8024–8032.
50. Baldwin, J., Krebs, C., Ley, B. A., Edmondson, D. E., Huynh, B. H., and Bollinger, J. M., Jr. (2000) Mechanism of rapid electron transfer during oxygen activation in the R2 subunit of *Escherichia coli* ribonucleotide reductase. 1. Evidence for a transient tryptophan radical. *J. Am. Chem. Soc. 122*, 12195–12206.
51. Solomon, E. I., Szilagyi, R. K., DeBeer George, S., and Basumallick, L. (2004) Electronic structures of metal sites in proteins and models: Contributions to function in blue copper proteins. *Chem. Rev. 104*, 419–458.
52. Walsh, C., Fisher, J., Spencer, R., Graham, D. W., Ashton, W. T., Brown, J. E., Brown, R. D., and Rogers, E. F. (1978) Chemical and enzymatic properties of riboflavin analogues. *Biochemistry 17*, 1942–1951.